Mon. Not. R. Astron. Soc. **000**, 1–12 (2012) Printed 14 April 2016 (MN LATEX style file v2.2)

The 154 MHz radio sky observed by the Murchison Widefield Array: noise, confusion and first source count analyses

T. M. O. Franzen[1] ∗, C. A. Jackson[1,2], A. R. Offringa[3], R. D. Ekers[1,2], R. B. Wayth[1,2], G. Bernardi[4,5,6], J. D. Bowman[7], F. Briggs[8,2], R. J. Cappallo[9], A. A. Deshpande[10], B. M. Gaensler[11,2,12], L. J. Greenhill[6], B. J. Hazelton[13], M. Johnston-Hollitt[14], D. L. Kaplan[15], C. J. Lonsdale[9], S. R. McWhirter[9], D. A. Mitchell[16,2], M. F. Morales[13], E. Morgan[17], J. Morgan[1], D. Oberoi[18], S. M. Ord[1,2], T. Prabu[10], N. Seymour[1], N. Udaya Shankar[10], K. S. Srivani[10], R. Subrahmanyan[10,2], S. J. Tingay[1,2], C. M. Trott[1,2], R. L. Webster[19,2], A. Williams[1] and C. L. Williams[17]

[1]*International Centre for Radio Astronomy Research, Curtin University, Bentley, WA 6102, Australia*
[2]*ARC Centre of Excellence for All-sky Astrophysics (CAASTRO)*
[3]*Netherlands Institute for Radio Astronomy (ASTRON), PO Box 2, 7990 AA Dwingeloo, The Netherlands*
[4]*SKA SA, 3rd Floor, The Park, Park Road, Pinelands, 7405, South Africa*
[5]*Department of Physics and Electronics, Rhodes University, PO Box 94, Grahamstown 6140, South Africa*
[6]*Harvard-Smithsonian Center for Astrophysics, 60 Garden Street, Cambridge, MA 02138, USA*
[7]*School of Earth and Space Exploration, Arizona State University, Tempe, AZ 85287, USA*
[8]*Research School of Astronomy and Astrophysics, Australian National University, Canberra, ACT 2611, Australia*
[9]*MIT Haystack Observatory, Westford, MA 01886, USA*
[10]*Raman Research Institute, Bangalore 560080, India*
[11]*Sydney Institute for Astronomy, School of Physics, The University of Sydney, NSW 2006, Australia*
[12]*Dunlap Institute for Astronomy and Astrophysics, University of Toronto, ON, M5S 3H4, Canada*
[13]*Department of Physics, University of Washington, Seattle, WA 98195, USA*
[14]*School of Chemical & Physical Sciences, Victoria University of Wellington, Wellington 6140, New Zealand*
[15]*Department of Physics, University of Wisconsin–Milwaukee, Milwaukee, WI 53201, USA*
[16]*CSIRO Astronomy and Space Science (CASS), PO Box 76, Epping, NSW 1710, Australia*
[17]*Kavli Institute for Astrophysics and Space Research, Massachusetts Institute of Technology, Cambridge, MA 02139, USA*
[18]*National Centre for Radio Astrophysics, Tata Institute for Fundamental Research, Pune 411007, India*
[19]*School of Physics, The University of Melbourne, Parkville, VIC 3010, Australia*

arXiv:1604.03751v1 [astro-ph.IM] 13 Apr 2016

Accepted ????. Received ????

ABSTRACT

We analyse a 154 MHz image made from a 12 h observation with the Murchison Widefield Array (MWA) to determine the noise contribution and behaviour of the source counts down to 30 mJy. The MWA image has a bandwidth of 30.72 MHz, a field-of-view within the half-power contour of the primary beam of 570 deg^2, a resolution of 2.3 arcmin and contains 13,458 sources above 5σ. The rms noise in the centre of the image is 4 – 5 mJy/beam. The MWA counts are in excellent agreement with counts from other instruments and are the most precise ever derived in the flux density range 30–200 mJy due to the sky area covered. Using the deepest available source count data, we find that the MWA image is affected by sidelobe confusion noise at the $\approx$ 3.5 mJy/beam level, due to incompletely-peeled and out-of-image sources, and classical confusion becomes apparent at $\approx$ 1.7 mJy/beam. This work highlights that (i) further improvements in ionospheric calibration and deconvolution imaging techniques would be required to probe to the classical confusion limit and (ii) the shape of low-frequency source counts, including any flattening towards lower flux densities, must be determined from deeper $\approx$ 150 MHz surveys as it cannot be directly inferred from higher frequency data.

Key words: catalogues — galaxies: active — radio continuum: galaxies — surveys

© 2012 RAS

∗Email: thomas.franzen@curtin.edu.au

1 INTRODUCTION

Radio source counts embody information about the extragalactic source populations and their evolution (i.e. space density) over cosmic time as determined by Longair (1966) and many others since. Whilst bright sources are relatively easy to identify, they are rare; the vast bulk of radio continuum emission emanates from moderate and low-power extragalactic radio sources whose radio emission is due to a central Active Galactic Nucleus (AGN) and/or ongoing star formation. These sources are distributed over a large range of redshifts, and thus contribute to the source counts to low flux densities. Surveys at a wide range of radio frequencies probe the faint sky, although at low frequencies (< 200 MHz), large-area (> 100 deg^2) surveys remain limited to confusion effects at the mJy level, mainly due to large instrumental beam sizes. The situation is expected to improve with the extensive baselines and sensitivity of the Low Frequency Array (LOFAR; van Haarlem et al. 2013) and Square Kilometre Array Low (Dewdney et al. 2012), which should push this limit substantially fainter.

Radio source counts can be used to derive the integrated sky brightness and the power spectrum signature of the extragalactic sources (e.g. Condon et al. 2012; Toffolatti et al. 1998). The typical sensitivity limit to which sources can be reliably extracted from a uniform survey is 5σ, where σ is due to the combination of confusion and system noise. However, even in fairly low resolution images where the noise is dominated by classical confusion, survey data can be statistically probed below the 5σ limit using the $P(D)$ (Scheuer 1957) distribution analysis to deduce the probable underlying source count behaviour (see e.g. Mitchell & Condon 1985; Condon et al. 2012). The large field-of-view (FoV) of the Murchison Widefield Array (MWA) and the huge number of detected sources gives rise to potential sidelobe confusion in images. Although we know that the deepest MWA images to date are confusion limited, the *relative* contribution of classical and sidelobe confusion is poorly determined: this makes it hard to statistically interpret survey data below the source detection threshold and to assess whether enhancements in the data processing, such as improved deconvolution techniques, have the potential to further reduce the noise.

Whilst our science driver is to determine the MWA radio source counts to probe the contributing extragalactic source populations and their evolution, these data are also important for analyses where these sources are considered contaminating foregrounds. A number of new instruments, including the MWA are seeking to detect the first global signals from the Epoch of Reionisation (EoR); these rely on direct foreground source subtraction or isolation of the composite foreground signal to isolate the much fainter EoR signal in the power spectra.

MWA EoR observations concentrate on fields selected at high Galactic latitude free of diffuse Galactic emission. There are two options to extracting the EoR signal from the foreground signals: (i) via direct foreground subtraction and (ii) via their statistical suppression within the power spectrum (see e.g. Morales & Hewitt 2004; Harker et al. 2010; Chapman et al. 2012; Trott, Wayth & Tingay 2012; Parsons et al. 2014). Both methods benefit from high-validity source catalogues, and for (ii), a significant extrapolation of the known source counts to model the behaviour of foreground sources to deep flux density limits to permit maximal analysis of the power spectrum.

In the absence of the availability of low frequency source counts, their behaviour has been deduced by extrapolating the counts at 1400 MHz, which are well determined to $\approx$10 μJy. This approach was used by Thyagarajan et al. (2013a) to estimate the level of foreground contamination expected in MWA EoR power spectra. However, adopting simple spectral index conversions is unreliable because the shape of the radio source counts changes with frequency due to the changing nature of the sources contributing to the counts at 1400 and 154 MHz, and the relative dominance of (any) flat-spectrum, beamed component(s) (see e.g. Wall (1994), Jackson & Wall (1999) and references therein).

In this paper, we use an image of one MWA EoR field (EoR0) to determine the 154 MHz source counts down to $\approx$ 30 mJy. We can probe the behaviour of classical and sidelobe confusion noise at S < 30 mJy by comparing with other source count data: this approach allows us to determine that the classical confusion noise becomes apparent at $\approx$ 1.7 mJy/beam and the sidelobe confusion noise can be expressed as a Gaussian distribution with rms $\approx$ 3.5 mJy/beam. Given that the sidelobe confusion noise is larger than the classical confusion limit, we do not attempt to extrapolate the behaviour of the 154 MHz source counts. Instead we investigate how sensitive our estimates are to a flattening in the source count slope below 6 mJy. In conclusion, we discuss likely origins of sidelobe confusion in MWA images and areas of future work.

2 MWA INSTRUMENT AND NOISE CHARACTERISTICS

The MWA is an interferometer comprised of 128 16-crossed-pair-dipole antenna 'tiles' distributed over an area $\approx$ 3 km in diameter. It operates at frequencies between 72 and 300 MHz, with an instantaneous bandwidth of 30.72 MHz. It is located at the Murchison Radio-astronomy Observatory in Western Australia and is the low-frequency precursor telescope for the SKA. We refer the reader to Lonsdale et al. (2009) and Tingay et al. (2013) for details of the technical design and specifications of the MWA. The primary science objectives of the MWA are detailed in Bowman et al. (2013). Using a uniform image weighting scheme, the angular resolution at 154 MHz is approximately 2.5 by 2.2 sec(δ + 26.7°) arcsec. Given the effective width ($\approx$ 4 m) of the MWA's antenna tiles, the primary beam FWHM is 27° at 154 MHz. The excellent snapshot *uv* coverage of the MWA, owing to the very large number (8128) of baselines, and its huge FoV allow it to rapidly image large areas of sky.

A key science goal for the MWA is to search for the redshifted 21-cm emission from the EoR in the early Universe. Several fields are being targeted with deep (accumulating up to 1000 h), pointed observations (see e.g. Beardsley et al. 2013). The confusion noise in these EoR images is worse than the thermal noise as we show in Section 5, making them ideal for measuring confusion. They also cover a sufficiently large area of sky to allow the source counts to be measured accurately over a wide range of flux densities.

There are three contributions to the total noise in all MWA images: system noise, classical confusion and sidelobe confusion, where we take sidelobe confusion to include calibration errors and smearing effects. In the remainder of this section, we briefly describe these in context of our current understanding of MWA observations.

2.1 Thermal noise

The Gaussian random noise term, $T_{\rm sys}$, is equal to $T_{\rm sky} + T_{\rm rec}$, where $T_{\rm sky}$ is the sky noise and $T_{\rm rec}$ the receiver noise. Given the low observing frequency of the MWA, $T_{\rm sys}$ is dominated by $T_{\rm sky}$, with a far

lower contribution from $T_{\rm rec}$. The thermal noise contribution in real MWA data can be estimated using an imaging mode with no confusion. Stokes V data are ideal providing identical aperture plane coverage and noise characteristics. In a single MWA 2 min snapshot at high Galactic latitude, for a central frequency of 154 MHz and a bandwidth of 30.72 MHz, the measured rms noise in uniformly weighted Stokes V images is $\approx$ 16 mJy/beam.

From Tingay et al. (2013), in theory, the naturally weighted sensitivity for the same integration time, central frequency and bandwidth is $\approx$ 5 mJy/beam (this assumes $T_{\rm sky}$ = 350 K and $T_{\rm rec}$ = 50 K). After accounting for a 2.1-fold loss in sensitivity due to uniform weighting (Wayth et al. 2015) and a reduction of $\approx$ 25 per cent in the bandwidth due to flagged edge channels, the theoretical prediction is $\frac{2.1}{\sqrt{0.75}} \times 5$ mJy/beam $\approx$ 12 mJy/beam, which compares well with our measurement above.

2.2 Classical confusion

Classical confusion occurs when the surface density of faint extragalactic sources is high enough to prevent the sources from being resolved by the array. The fluctuations in the image are due to the sum of all sources in the main lobe of the synthesised beam. Classical confusion only depends on the source counts and the synthesised beam area (Condon 1974).

Bernardi et al. (2009) used a power spectrum analysis to estimate the classical confusion noise in three 6×6 deg^2 sky areas observed with the Westerbork Synthesis Radio Telescope at 150 MHz. They estimated the rms classical confusion noise at 150 MHz, $\sigma_{\rm c}$, to be 3 mJy/beam for a 2 arcmin beam. Other analyses to estimate the MWA classical confusion limit have extrapolated higher frequency source counts given the paucity of deep 150 MHz source count data and have adopted slightly different beam size estimates. Using the method described in Thyagarajan et al. (2013a), Thyagarajan (2013b) estimated $\sigma_{\rm c}$ from extrapolation of the 1400 MHz counts by Hopkins et al. (2003) to 150 MHz. Assuming $\alpha_{150}^{1400} = -0.78$ ($S \propto \nu^{\alpha}$) and a source subtraction limit of 5σ, they obtained $\sigma_{\rm c}$ = 3 mJy/beam for a 2 arcmin beam. Wayth et al. (2015) estimated $\sigma_{\rm c}$ from extrapolation of the 327 MHz counts measured by Wieringa (1991) down to 4 mJy. Following Condon and using a signal-to-noise threshold of 6, Wayth et al. obtained $\sigma_{\rm c}$ = 2 mJy/beam for a 2.4 arcmin beam.

LOFAR EoR observations are probing the 115–190 MHz sky to $\approx$ 30 μJy/beam rms, although no deep extragalactic source catalogues are yet available. Observations with the Giant Metrewave Radio Telescope (GMRT) by Intema et al. (2011), Ghosh et al. (2012) and Williams, Intema & Röttgering (2013) probe the 153 MHz counts down to 6, 12 and 15 mJy, respectively. In Section 5, we use these deep source counts to quantify the classical confusion noise in the MWA data.

2.3 Sidelobe confusion

Sidelobe confusion introduces additional noise into an image due to imperfect source deconvolution within the image; i.e. by all sources below the source subtraction cut-off limit and also from the array response to sources outside the imaged FoV. The MWA array has an irregular layout (i.e. station baselines are unique) and performs a huge number (8128) of correlations such that sidelobes from any single short observation will be randomly distributed and hard to distinguish from real sources or other noise elements.

The top panel of Fig. 1 shows the central square degree of the MWA synthesised beam for a 2 min snapshot with a central frequency of 154 MHz and bandwidth of 30.72 MHz, using a uniform weighting scheme. The standard deviation of the beam drops from $\approx 1.3 \times 10^{-2}$ at a distance of 10 arcmin from the beam centre to $\approx 3.5 \times 10^{-4}$ at a distance of 13.5 deg from the beam centre (i.e. at the half-power point), as shown in the bottom panel of Fig. 1.

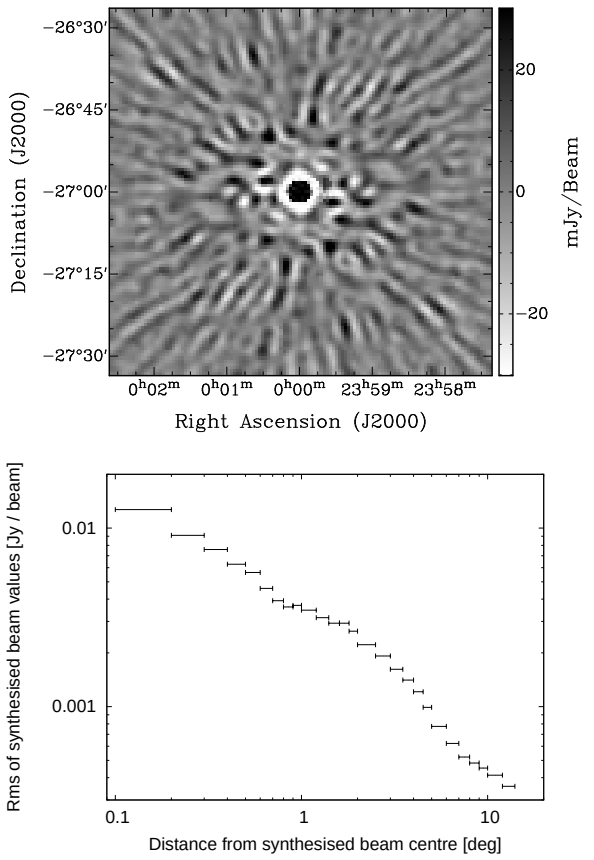

Figure 1. Top: central square degree of the MWA synthesised beam for a 2 min snapshot with a central frequency of 154 MHz and bandwidth of 30.72 MHz, using a uniform weighting scheme. The peak is 1 Jy/beam and the greyscale runs from –30 to 30 mJy/beam. The main lobe of the synthesised beam is saturated to clearly show the distant sidelobe structure. Bottom: standard deviation of the pixel values in the beam as a function of distance from the beam centre. This standard deviation was calculated in a thin annulus at the given radius.

3 MWA EOR DATA

Offringa et al. (2016) explored the effect of foreground spectra on EoR experiments by measuring spectra with high frequency resolution for the 586 brightest unresolved sources in the MWA EoR0 field, centred at J2000 $\alpha = 00^{\rm h}00^{\rm m}00^{\rm s}$, $\delta = -27^{\circ}00'00''$. The observations used in their work were spread over 12 nights between 2013 August and 2013 October. They were made in two frequency bands covering 139 – 170 MHz and 167 – 198 MHz, with a frequency resolution of 40 kHz and time resolution of 0.5 s.

The mean rms noise over the central 10 degrees of the Stokes I image integrated over the total 59 MHz bandwidth was 3.6 mJy/beam after 5 h of integration. The rms noise continued to decline after 5 h of integration but not proportionally to $1/\sqrt{t}$: an

rms noise of 3.2 mJy/beam was reached after 45 h of integration. The rms noise in the Stokes V image continued to follow $1/\sqrt{t}$, reaching a level of 0.6 mJy/beam after 45 h of integration. The Stokes V image was void of sources, except for weak sources that appeared because of instrumental leakage. The Stokes V leakage was typically 0.1 – 1 per cent of the Stokes I flux density.

The image analysed in this paper was made from a 12 h subset of the low band data presented in Offringa et al. (2016), observed over three nights in 2013 September. The image, corrected for the primary beam, is shown in Fig. 2. The primary beam FWHM is 27 deg and the resolution is 2.3 arcmin. The region of the field within the primary beam FWHM covers an area of 570 deg^2.

The data processing strategy is described in detail in Offringa et al. (2016) and summarised here. Briefly, the COTTER preprocessing pipeline (Offringa et al. 2015) was used to flag RFI, average the data in time to 4 s and convert the raw data to measurement sets; no frequency averaging was performed. Initial calibration was performed as a direction-independent full-polarisation self-calibration. The source model was primarily based on the MWA Commissioning Survey (Hurley-Walker et al. 2014) at 180 MHz and the Sydney University Molonglo Sky Survey (SUMSS; Mauch et al. 2003) at 843 MHz. A few thousand sources with apparent flux densities greater than 100 mJy, and a few complex sources, were peeled using a direction-dependent peeling procedure that mitigates the ionosphere. The peeled snapshots were imaged with uniform weighting using WSClean (Offringa et al. 2014). Each snapshot was CLEANed to a depth of 100 mJy/beam. The snapshots were corrected for the primary beam and mosaicked together. Finally, the peeled sources were added back into the mosaicked image and restored with a Gaussian beam.

As described above, the EoR imaging process weights and adds a number of two minute snapshots. As each snapshot is short, the aperture plane is incompletely sampled such that all detected sources generate sidelobes. Each snapshot is imaged separately with the sources being deconvolved to a limit of about 4 times the typical rms of each snapshot. Whilst sidelobe confusion reduces as sources are extracted, there is a limit; eventually the sidelobe terms exceed those from real sources and any further CLEAN iterations will diverge rather than improve the imaging process. As a result, sidelobes from the fainter sources plus those from sources outside the imaged FoV remain in the snapshot images. The mosaicking process (weighted average of N snapshots) reduces the thermal noise and improves the synthesised beam. However, as neither the fainter sources nor the far-field sources have been deconvolved in the individual snapshots, their sidelobes remain in the mosaic.

The peeling procedure more accurately characterises the synthesised beam sidelobes than CLEANing (see Offringa et al. 2016). This reduction in sidelobe contamination due to peeling makes a substantial improvement to the final image.

4 DETERMINING THE 154 MHz SOURCE COUNTS

We used the MWA EoR image described in Section 3 to construct a source catalogue and measure the 154 MHz counts. We first used BANE[1] to remove the background structure and estimate the noise across the image. The 'box' parameter defining the angular scale on which the rms and background are evaluated was set to 20 times the synthesised beam size. The mean rms noise over the central 10 degrees of the image is 4.6 mJy/beam. The background map is shown in Fig. 3. Large-scale fluctuations correspond to Galactic structure in that their position is constant with frequency and they correspond to increased flux density in the Continuum HI Parkes All Sky Survey map (Calabretta, Staveley-Smith & Barnes 2014). The mean background within the half-power beamwidth is –2.7 mJy/beam. We then ran the source finder AEGEAN (Hancock et al. 2012), detecting 13,458 sources above 5σ within 13.5 deg radius from the pointing centre.

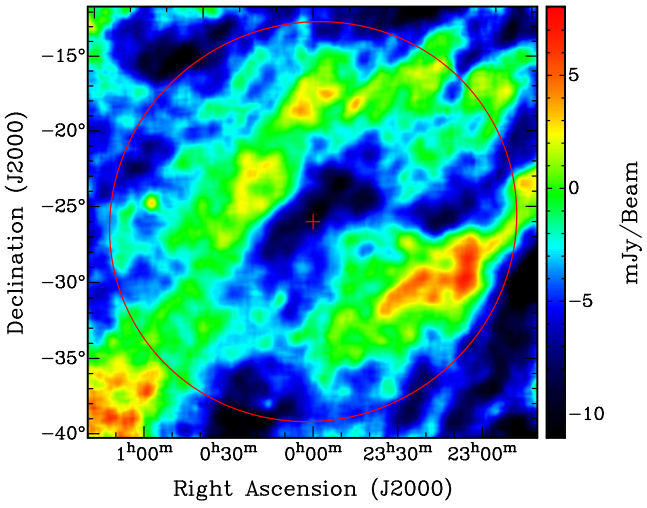

Figure 3. The background map created by running BANE on the EoR0 field. The red cross shows the pointing centre and the red circle the half-power beamwidth. The colour scale is linear and runs from –11 to 8 mJy/beam.

Given that the vast majority of sources are unresolved due to the large beam size, we used the peak flux densities to measure the counts. Source blending may significantly affect the counts because of the low number (25) of beams per source. We followed a similar method to that employed by Gower (1966) for the 4C survey to quantify the effect of both source blending and incompleteness on the counts. We injected artificial point sources drawn from a source count model into the real image and measured the flux densities of the simulated sources using the same techniques as for the real source list. The corrections to the counts were obtained by comparing the measured counts of the simulated sources with the source count model.

The source count model used was a 5th order polynomial fit to the 7C counts (Hales et al. 2007) at 151 MHz and the GMRT counts by Intema et al. (2011), Ghosh et al. (2012) and Williams, Intema & Röttgering (2013) at 153 MHz. As these counts are measured at very similar frequencies, we neglect any correction to transpose them to 154 MHz as the effect will be inconsequential; henceforth, when referring to the 7C and GMRT counts, we consider them to be measured at 154 MHz. A total of 32,120 sources with flux densities ranging between 6 mJy and 100 Jy were injected into the region of the field within the primary beam FWHM using the MIRIAD task IMGEN. The positions of the simulated sources were chosen randomly; to avoid the simulated sources affecting each other, a simulated source was not permitted to lie within 10 ar-

[1] https://github.com/PaulHancock/Aegean

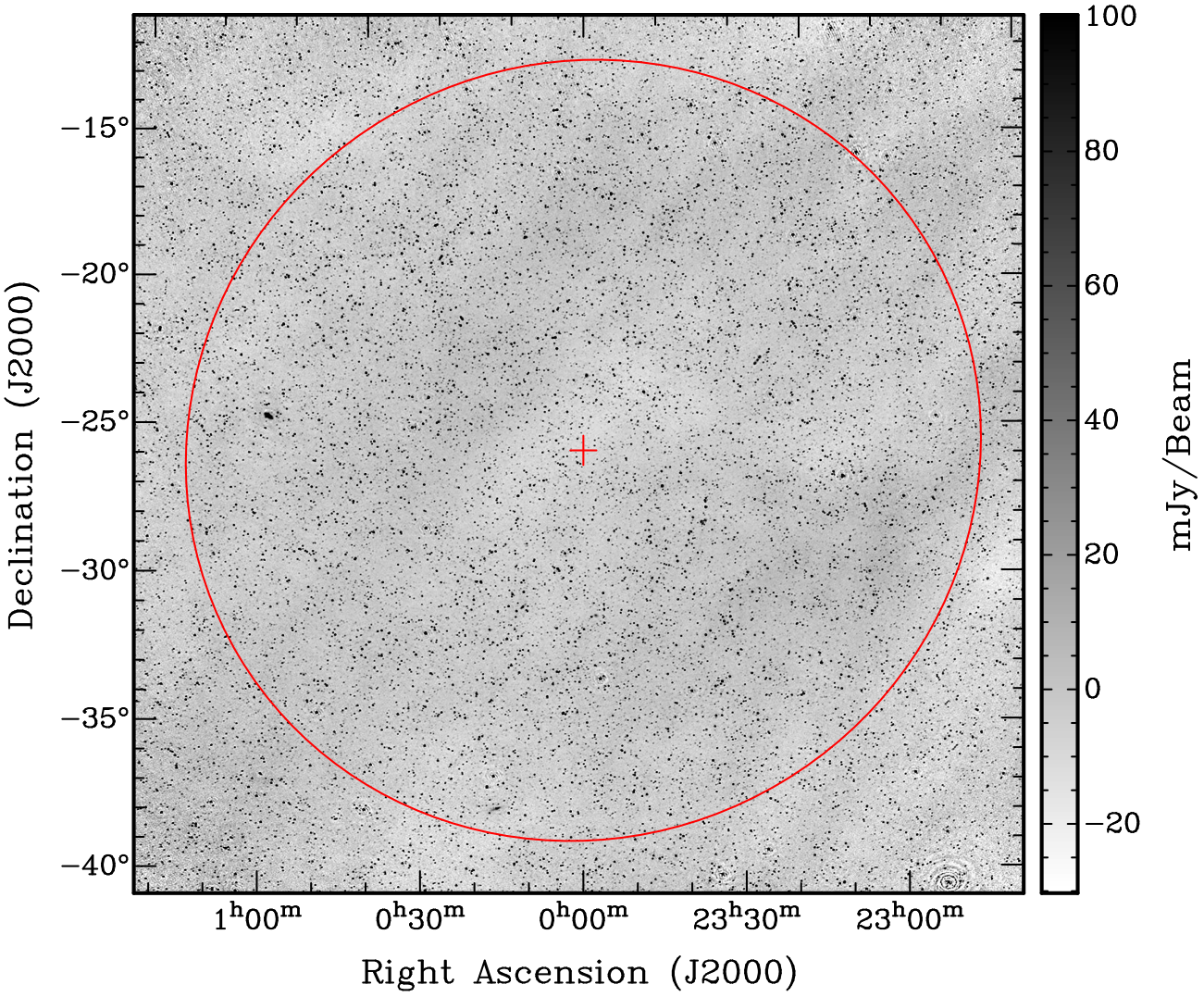

Figure 2. Image of the EoR0 field. The red cross shows the pointing centre and the red circle the half-power beamwidth. The greyscale is linear and runs from –30 to 100 mJy/beam.

cmin from any other and only 3,212 sources were injected into the image at a time.

In cases where a simulated source was found to lie too close to a real source to be detected separately, the simulated source was considered to be detected if the recovered source position was closer to the simulated rather than the real source position. The Monte Carlo analysis therefore accounts for sources which are omitted from the source finding process through being too close to a brighter source.

These simulations were repeated 100 times to improve statistics. Fig. 4 shows the mean correction factor to be applied to the counts in each flux density bin. The error bars are standard errors of the mean. The gradual increase in the correction factor between ≈ 1 Jy and ≈ 40 mJy is due to source confusion; the effect of confusion is to steepen the slope of the counts. The sharp increase in the correction factor below ≈ 40 mJy is due to incompleteness.

Our MWA differential source count data corrected for incompleteness and source blending are provided in Table 1. Fig. 5 shows the MWA counts compared with the 7C and GMRT counts. We find that the MWA counts are in excellent agreement with the other

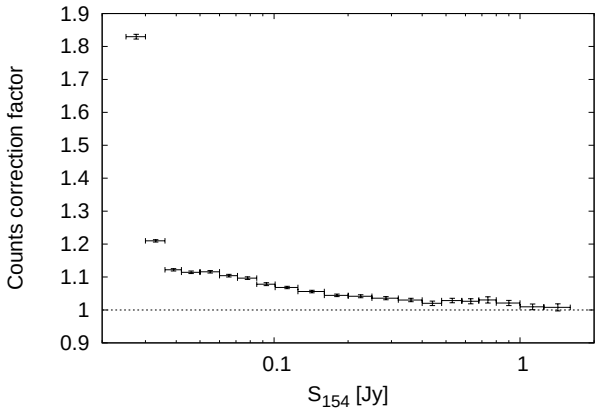

Figure 4. Top: Source count correction factor as a function of flux density, accounting for both source confusion and incompleteness.

counts despite the lower MWA resolution: in comparison, the 7C survey has a resolution of 70 arcsec and the GMRT observations have resolutions ranging between 20 and 25 arcsec. This indicates that the flux density scale of the MWA image, based on the MWA Commissioning Survey (Hurley-Walker et al. 2014), is fully consistent with the 7C survey and the deeper GMRT data. The MWA counts are by far the most precise in the flux density range 30–200 mJy as a result of the large area of sky covered (570 deg^2). The surveys used to derive the GMRT counts cover areas ranging between 6.6 and 30 deg^2.

5 QUANTIFYING THE CLASSICAL AND SIDELOBE CONFUSION NOISE

We use the method of probability of deflection, or $P(D)$ analysis, to quantify the classical and sidelobe confusion in the MWA EoR image. We also investigate the effect of image artefacts caused by calibration errors on the pixel statistics, and estimate the degree of bandwidth and time-average smearing in the image.

The deflection D at any pixel in the image is the intensity in units of mJy/beam. We assume that the observed $P(D)$ distribution is given by

$$P_o(D) = P_n(D) * P_c(D) * P_s(D), \quad (1)$$

where '$*$' represents convolution, $P_n(D)$ is the $P(D)$ distribution resulting from the Gaussian system noise, $P_c(D)$ is the $P(D)$ distribution from all sources present in the image given the synthesised beam size and $P_s(D)$ is the $P(D)$ distribution from residual sidelobes. We take $P_s(D)$ to include image artefacts due to calibration errors and smearing effects.

Below 400 mJy, the Euclidean normalised differential counts at 154 MHz from Williams, Intema & Röttgering (2013), Intema et al. (2011) and Ghosh et al. (2012) are well represented by a power law of the form $\frac{dN}{dS} = kS^{-\gamma}$ Jy^{-1}sr^{-1}, with $k = 6998$ and $\gamma = 1.54$ (see dashed diagonal line in Fig. 5). In these data we see that the 154 MHz differential source counts continue to decline at $S_{154} \lesssim 10$ mJy. Any flattening towards low flux densities, seen at higher frequencies, has not yet been detected.

We derived $P_c(D)$ for this source count model fit as follows: we simulated a 9.63 by 9.63 deg noise-free image containing point sources at random positions, randomly assigning their flux densities from the power-law fit. A total of 51,887 sources with flux densities ranging between 0.1 and 400 mJy were injected into the image. The simulated point sources were convolved with the Gaussian restoring beam; we did not attempt to model the sidelobe confusion. Although our source count model fit is valid between 6 and 400 mJy, we assumed no change in the source count slope below 6 mJy. In Section 6, we explore the effect of a flattening in the counts below 6 mJy on the classical confusion noise. We obtained $P_c(D)$ from the distribution of pixel values in the simulated image.

Fig. 6 shows the derived source $P(D)$ distribution. The width of this distribution is 1.7 mJy/beam, as measured by dividing the interquartile range by 1.349, i.e. the rms for a Gaussian distribution. As noted by Zwart et al. (2015), source $P(D)$ distributions are usually highly skewed and very non-Gaussian. Although we have quoted the core width of the distribution, we caution that a single descriptor is unsuitable. Of course, the advantage of a $P(D)$ analysis is that it accounts for the exact shape of the distribution.

Fig. 7 shows $P_c(D)$, $P_n(D)$ as represented by the pixel distribution in the Stokes V image, $P_o(D)$ as represented by the pixel distribution in the Stokes I image and $P_c(D) * P_n(D)$. If the source

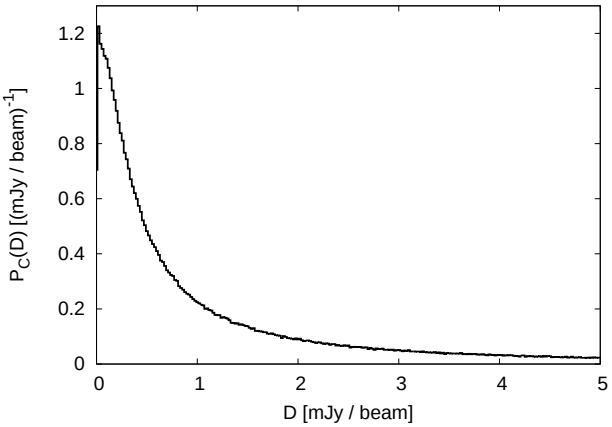

Figure 6. $P_c(D)$ assuming the extrapolated source count fit of Fig. 5 and a Gaussian beam of size 2.31 arcmin FWHM, calculated as discussed in Section 5.

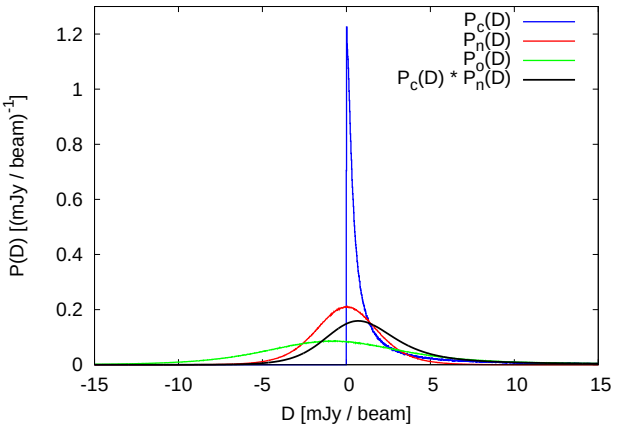

Figure 7. Source $P(D)$ distribution as in Fig. 6 (blue), pixel distribution in the Stokes V image, representing the system noise distribution (red), pixel distribution in the Stokes I image (green) and convolution of the source $P(D)$ distribution with the system noise distribution (black).

count model is correct and the sidelobe confusion is negligible, $P_c(D) * P_n(D)$ would agree with $P_o(D)$.

However, as can be seen in Fig. 7 this is not the case, and requires further interpretation: the image zero-point $D = 0$ can be treated as a free parameter when comparing the observed $P(D)$ distribution with models of the source $P(D)$ distribution (the background was subtracted from the real image, and in any case, interferometers have no sensitivity to large-scale emission). Fig. 8 compares $P_c(D) * P_n(D)$ with $P_o(D)$ after removing an offset of 1.88 mJy/beam in the x-direction between the two curves, where there remains very poor agreement. Given the excellent *uv* coverage of the MWA and the huge number of sources present in the FoV, it is reasonable to expect the sidelobe confusion noise to be roughly Gaussian. Indeed, we examined the distribution of pixel values in 27 thin annuli centred on the synthesised beam with radii ranging between 0.15 and 13 deg. In each case, the distribution of pixel values was found to be approximately Gaussian. Fig. 9 shows the distribution at the two extremes.

We subsequently convolved $P_c(D) * P_n(D)$ with a Gaussian with rms = 3.5 mJy/beam, obtaining the red curve in Fig. 8, which

Table 1. Differential counts at 154 MHz in EoR0 from the MWA image. The counts are corrected for incompleteness and source blending as described in the text. The bin centre corresponds to the mean flux density of all sources in each bin. In the two highest flux density bins which contain less than 20 sources each, we use approximate formulae for confidence limits based on Poisson statistics by Gehrels (1986). In the remaining bins, the Poisson error on the number of sources is approximated as the square root of the number of sources.

Bin start S (Jy)	Bin end S (Jy)	Bin centre S (Jy)	Number of sources	Correction factor	Euclidean normalised counts ($\mathrm{Jy}^{3/2}\mathrm{sr}^{-1}$)
7.00	10.00	8.12	8	-	2884^{1428}_{-997}
5.00	7.00	5.92	14	-	3431^{1186}_{-905}
3.50	5.00	4.15	32	-	4315 ± 763
2.50	3.50	2.96	49	-	4269 ± 610
2.00	2.50	2.21	37	-	3101 ± 510
1.60	2.00	1.78	58	-	3506 ± 460
1.25	1.60	1.40	119	1.008 ± 0.011	4599 ± 424
1.00	1.25	1.11	140	1.010 ± 0.009	4211 ± 358
0.800	1.000	0.892	143	1.021 ± 0.008	3157 ± 265
0.680	0.800	0.735	137	1.031 ± 0.010	3135 ± 269
0.580	0.680	0.628	164	1.026 ± 0.008	3032 ± 238
0.480	0.580	0.524	201	1.029 ± 0.007	2366 ± 168
0.400	0.480	0.437	252	1.020 ± 0.007	2342 ± 148
0.320	0.400	0.357	390	1.030 ± 0.005	2198 ± 112
0.250	0.320	0.284	482	1.036 ± 0.005	1764 ± 81
0.200	0.250	0.223	567	1.042 ± 0.004	1597 ± 67
0.160	0.200	0.180	621	1.044 ± 0.004	1275 ± 51
0.125	0.160	0.141	793	1.056 ± 0.004	1024 ± 37
0.101	0.125	0.112	829	1.068 ± 0.004	893 ± 31
0.085	0.101	0.0925	795	1.078 ± 0.004	803 ± 29
0.071	0.085	0.0777	833	1.097 ± 0.004	632 ± 22
0.060	0.071	0.0652	916	1.104 ± 0.004	574 ± 19
0.050	0.060	0.0548	1141	1.116 ± 0.004	516 ± 15
0.042	0.050	0.0458	1129	1.114 ± 0.004	407 ± 12
0.036	0.042	0.0390	1090	1.122 ± 0.004	352 ± 11
0.030	0.036	0.0331	1284	1.210 ± 0.004	297 ± 8

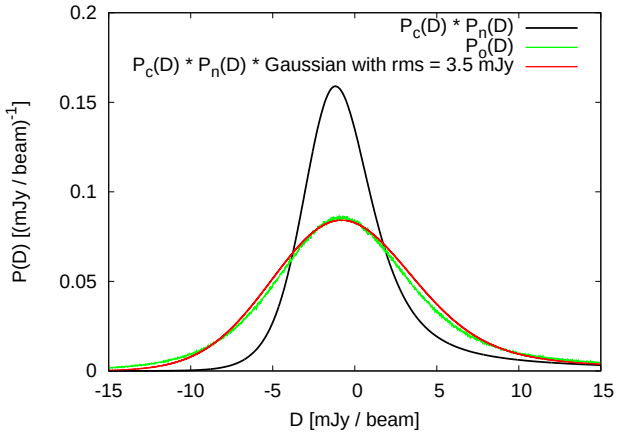

Figure 8. The green curve shows $P_{\rm o}(D)$, the black curve shows $P_{\rm c}(D) * P_{\rm n}(D)$, shifted by 1.88 mJy/beam to the left to remove the offset in the x-direction with respect to $P_{\rm o}(D)$, and the red curve shows the black curve convolved with a Gaussian with rms = 3.5 mJy/beam; this Gaussian is taken to represent $P_{\rm s}(D)$.

is very close to $P_{\rm o}(D)$. We therefore conclude that the sidelobe confusion noise is ≈ 3.5 mJy/beam, on the assumption that the extrapolated ($S < 6$ mJy) source count model remains valid.

5.1 Calibration artefacts

There is an increased level of noise around the brightest sources in the field due to calibration errors (see Fig. 10). The rms in the vicinity of sources above 5 Jy, lying within the half-power beamwidth, is typically 0.1 per cent of the source's peak flux density. For a source of peak flux density $S_{\rm pk}$, the noise was found to be elevated within a distance R from the source, where

$$R = 5\left(S_{\rm pk}/\mathrm{Jy}\right)^{1/2} \ \mathrm{arcmin}. \qquad (2)$$

We repeated the analysis described in Section 5 after masking all pixels in the Stokes I image lying within distance R from sources with $S_{\rm pk} > 5.0$ Jy. The fraction of pixels excised from the map was 1.1 per cent. We obtained $\sigma_{\rm s} = 3.4$ mJy/beam, which is very close to our estimate of $\sigma_{\rm s}$ (3.5 mJy/beam) in the original image, indicating that calibration artefacts have a negligible effect on $\sigma_{\rm s}$.

5.2 Wide-field imaging effects

Assuming a Gaussian beam and rectangular bandpass, bandwidth smearing causes the peak flux density of a point source in an individual snapshot to be multiplied by

$$\alpha = \left[1 + \frac{2\ln 2}{3}\left(\frac{\Delta\nu_{\rm eff}}{\nu}\frac{d}{\theta}\right)\right]^{-\frac{1}{2}} \leqslant 1\,, \qquad (3)$$

where $\Delta\nu_{\rm eff}$ is the effective channel bandwidth, ν the central frequency, d the radial distance from the phase centre and θ the

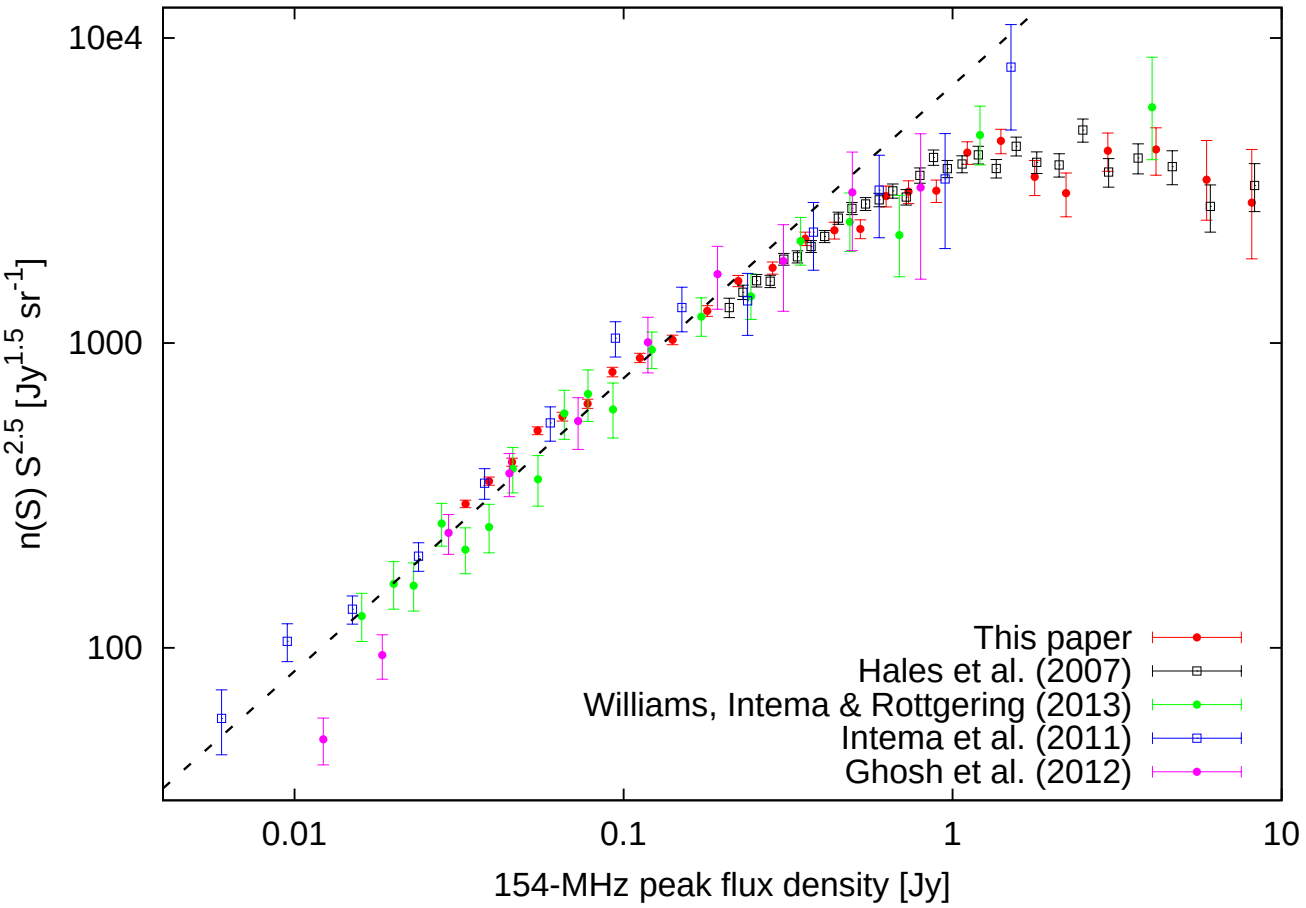

Figure 5. Euclidean normalised ($S^{2.5}\frac{dN}{dS}$) differential counts at 154 MHz. Red circles: this paper; black squares: Hales et al. (2007); green circles: Williams, Intema & Röttgering (2013); blue squares: Intema et al. (2011); purple circles: Ghosh et al. (2012). The dashed diagonal line shows a weighted least-squares power-law fit ($\frac{dN}{dS} = 6998\,S^{-1.54}$ Jy^{-1}sr^{-1}) to the GMRT data from Williams, Intema & Röttgering (2013), Intema et al. (2011) and Ghosh et al. (2012) below 400 mJy.

synthesised beam FWHM (Condon et al. 1998). The width of the source in the radial direction is divided by α. For $\delta\nu = 40$ kHz, $\nu = 154$ MHz, $\theta = 2.31$ arcmin and $d = 13.5$ deg, i.e. at the half-power point, $\alpha = 0.980$. Given that each snapshot was weighted by the square of its primary beam response in the mosaicking process, we have established that $0.980 < \alpha < 1$ in the final mosaicked image within 13.5 deg from the image centre. The bandwidth smearing effect is small and cannot contribute significantly to $P_s(D)$.

For uniform circular uv coverage, time-average smearing causes the peak flux density of a point source near the North or South Celestial Pole to be multiplied by

$$\beta = 1 - 1.08 \times 10^{-9} \left(\frac{d}{\theta}\right)^2 \tau^2 \leqslant 1\,, \qquad (4)$$

where τ is the averaging time (Bridle & Schwab 1999). The width of the source in the azimuthal direction is divided by β. For $\tau = 4$ s, $\theta = 2.31$ arcmin, and $d = 13.5$ deg, $\beta = 0.998$. The time-average smearing effect is even smaller than the bandwidth smearing effect.

6 EXTENDING THE OBSERVED 154 MHz SOURCE COUNT

While there is a steep slope across the 6–400 mJy 154 MHz Euclidean normalised differential source counts (see Fig. 5), it is posited that this will flatten if there is a sizeable, fainter source population at $S_{154\,\mathrm{MHz}} \lesssim 10$ mJy (Jackson 2005). This behaviour would mirror the flattening of the 1400 MHz source counts at $S_{1400} \lesssim 2$ mJy. Previous work has adopted a spectral index $\alpha \approx -0.7$ ($S \propto \nu^{\alpha}$), the canonical value for optically-thin synchrotron radiation, to extrapolate from 1400 to 154 MHz to predict the low frequency sky, but this could be naïve: it assumes that the fainter population observed at 1400 MHz is indeed present at 154 MHz and has a typical spectral index of –0.7, and also that there is no low frequency source population with very steep spectra which is undetected at 1400 MHz.

In fact, Appendix A clearly demonstrates the problems inherent in using deep 1400 MHz catalogues to predict the sky at a much lower frequency. The 154 MHz counts, which are well characterised down to $\approx$ 6 mJy, cannot be accurately predicted from 1400 MHz counts using simple spectral index conversions. It is well known that a survey at higher/lower frequency prefer-

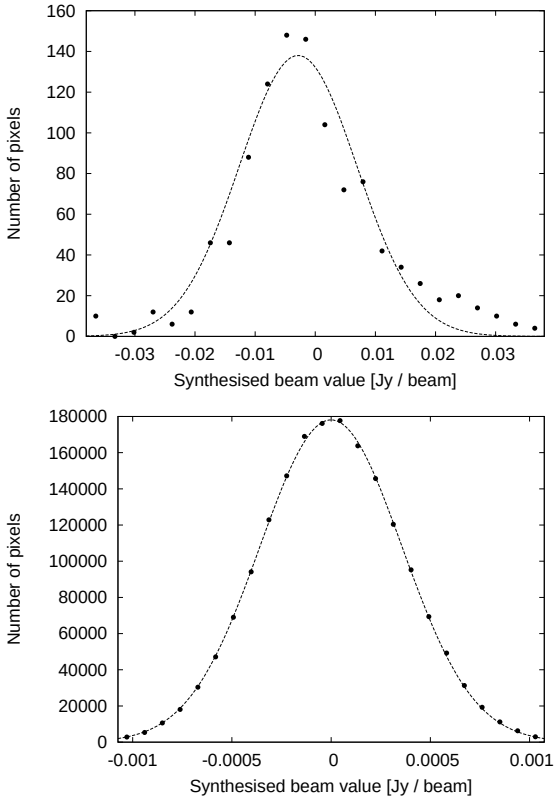

Figure 9. Top: the circles show the distribution of synthesised beam pixel values in an annulus centred on the beam with inner and outer radii of 0.1 and 0.2 deg, respectively. The dashed line is a least-squares Gaussian fit to the data points. Bottom: distribution of synthesised beam pixel values in an annulus centred on the beam with inner and outer radii of 12 and 14 deg, respectively.

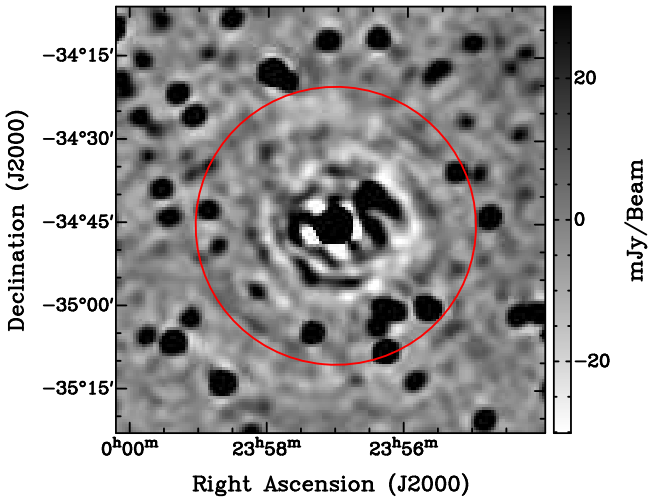

Figure 10. Section of the EoR field centred on a 24.3 Jy source. Small errors in the amplitude and phase calibration of the visibility data lead to artefacts in the image. The subsequent exclusion region around this source is shown as a red circle.

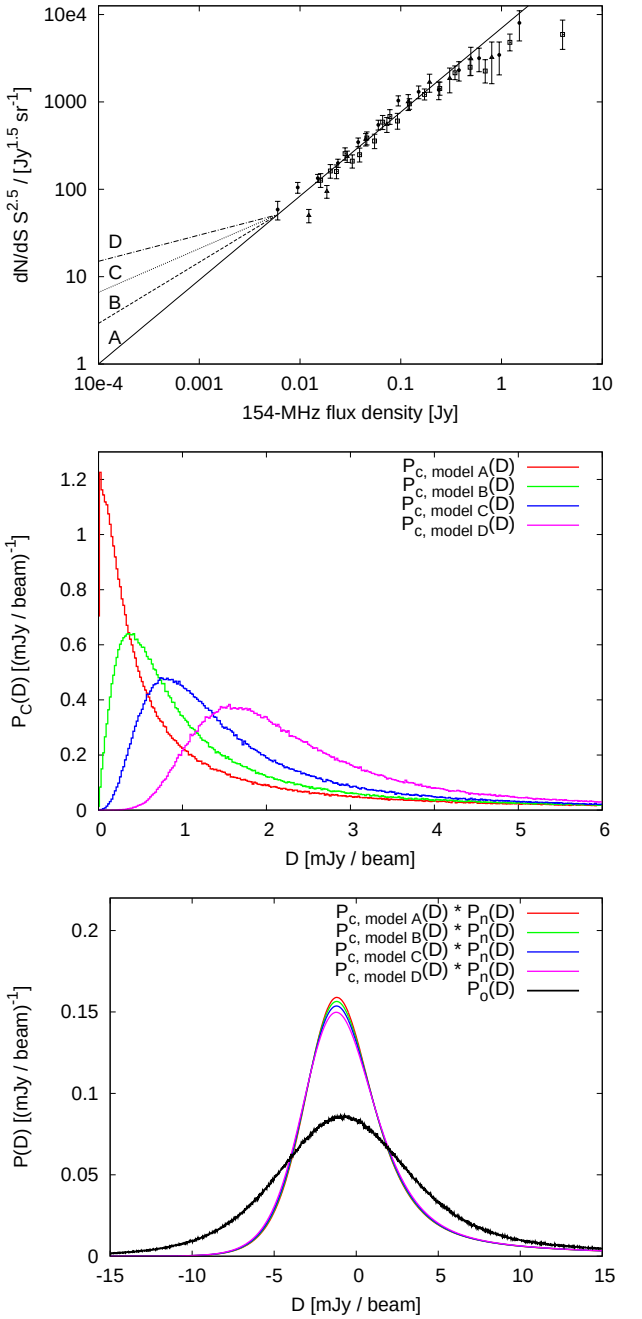

Figure 11. Top: The squares, circles and triangles show the 154 MHz counts by Williams, Intema & Röttgering (2013), Intema et al. (2011) and Ghosh et al. (2012), respectively. The solid, dashed, dotted and dot-dashed lines show source count models A, B, C and D, respectively. Middle: $P_c(D)$ distributions corresponding to source count models A–D, using a Gaussian beam with FWHM = 2.31 arcmin. The rms values of these distributions are quoted in Table 2. Bottom: observed $P_o(D)$ distribution (black), $P_c(D)$ distributions for models A (red), B (green), C (blue) and D (purple), convolved with the noise $P_n(D)$ distribution and shifted to the left to remove offsets in the x-direction with respect to $P_o(D)$.

entially detects sources with flatter/steeper spectra. This selection bias, which was first analysed in detail by Kellermann (1964), causes the effective spectral index distribution to change with frequency, which in turn renders simple extrapolations of counts invalid.

For this reason, we chose not to extrapolate the 1400 MHz counts to 154 MHz to model the deep 154 MHz counts. We explored three additional source count models, setting the source count slope below 6 mJy to 1.8 (model B), 2.0 (model C) and 2.2 (model D). Model A corresponds to the case explored above where there is no flattening in the counts below 6 mJy. The counts are modelled as

$$n(S) \equiv \frac{\mathrm{d}N}{\mathrm{d}S} \approx \begin{cases} k_1 \left(\frac{S}{\mathrm{Jy}}\right)^{-\gamma_1} \ \mathrm{Jy}^{-1}\ \mathrm{sr}^{-1} \text{ for } S_{\mathrm{low}} \leqslant S < S_{\mathrm{mid}} \\ k_2 \left(\frac{S}{\mathrm{Jy}}\right)^{-\gamma_2} \ \mathrm{Jy}^{-1}\ \mathrm{sr}^{-1} \text{ for } S_{\mathrm{mid}} \leqslant S \leqslant S_{\mathrm{high}}\,. \end{cases} \quad (5)$$

The values of the source count parameters k_1, γ_1, k_2, γ_2, S_{low}, S_{mid} and S_{high} for each model are provided in Table 2.

Source count models A–D are shown in the top panel of Fig. 11. The middle panel of Fig. 11 shows the $P(D)$ distributions corresponding to these source count models. The bottom panel of Fig. 11 shows these distributions convolved with the system noise distribution and shifted to the left to remove offsets in the x-direction with respect to the observed $P(D)$ distribution. Table 2 shows the predicted values of σ_{c} and σ_{s} for each source count model. σ_{c} and σ_{s} appear to be relatively insensitive to the slope of the counts below 6 mJy. This indicates that sources below this flux density level are too faint to contribute significantly to the confusion noise at this resolution. Table 3 shows the predicted source densities at 154 MHz above 5, 1, 0.5, 0.1 and 0.03 mJy/beam, for each source count model.

7 DISCUSSION AND FUTURE WORK

We have analysed an MWA image of the EoR0 field at 154 MHz with 2.3 arcmin resolution to determine the noise contribution and behaviour of the source counts down to 30 mJy. The MWA EoR0 counts are in excellent agreement with the 7C counts by Hales et al. (2007) and GMRT counts by Williams, Intema & Röttgering (2013), Intema et al. (2011) and Ghosh et al. (2012); our measurements are by far the most precise in the flux density range 30–200 mJy as a result of the large area of sky covered. The differential GMRT counts are well represented by a power law of the form $\frac{dN}{dS} = 6998\ S^{-1.54}\,\mathrm{Jy}^{-1}\mathrm{sr}^{-1}$ between 6 and 400 mJy. Assuming no change in the slope of the 154 MHz counts below 6 mJy, we estimate the classical confusion noise to be $\approx$ 1.7 mJy/beam and the sidelobe confusion noise to be $\approx$ 3.5 mJy/beam; the predicted classical and sidelobe confusion noise is relatively insensitive to the slope of the counts below 6 mJy.

Our $P(D)$ analysis suggests that, in this MWA EoR0 image, sidelobe confusion dominates other noise contributions despite the excellent *uv* coverage. This is a consequence of the large FoV and the huge number of detected sources. We have identified three aspects of the data processing which potentially contribute to the sidelobe confusion in these types of MWA images:

(1) The limited CLEANing depth. The snapshot images were CLEANed separately down to 100 mJy/beam before mosaicking, which is 22 times the rms noise (4.5 mJy/beam) in the final mosaicked image. In practice, while CLEANing the image deeper is likely to lower the sidelobe confusion noise, ionospheric perturbations and primary beam-model errors introduce limitations in the ability to deconvolve the image, making other approaches such as peeling more viable than deeper CLEANing.

(2) Far-field sources that have not been deconvolved: only the central 40 by 40 deg region of the image has been fully deconvolved, and peeling limited to sources within 20 deg from the pointing centre. The importance of this effect will critically depend on how rapidly the rms of the MWA's synthesised beam decreases with distance from the beam centre.

(3) Source smearing due to the ionosphere. In each snapshot image, the ionosphere introduces a random displacement (typically 10–20 arcsec) in the source positions (Loi et al. 2015). This smears out sources in the mosaicked image. Peeling corrects for the ionosphere whereas CLEANing does not.

It is unclear which of these factors is dominant; this will be the subject of further work.

Unlike previous estimates of the MWA classical confusion limit by Thyagarajan (2013b) and Wayth et al. (2015), our estimates do not rely on extrapolation of higher frequency counts, and we derive the exact shape of the source $P(D)$ distribution. In Appendix A, we show that the 154 MHz counts cannot be accurately reproduced from extrapolation of the 1400 MHz counts using simple spectral index conversions, demonstrating the need for deep source counts at the same frequency as EoR observations rather than extrapolating from higher frequencies.

We plan to apply our $P(D)$ analysis to images from the GaLactic Extragalactic All-sky MWA (GLEAM; Wayth et al. 2015) survey to assess how the different observing strategy and processing techniques affect sidelobe confusion. In so doing, we will quantify the magnitude of ionospheric smearing in detail. The GLEAM survey covers the entire sky south of declination +25° at 72–231 MHz, reaching a sensitivity of $\approx$ 5 mJy/beam. We will also compare EoR specific imaging techniques to assess the impact of sidelobe confusion in detail, including Fast Holographic Deconvolution (Sullivan et al. 2012) and the Real-Time System (Mitchell et al. 2008; Ord et al. 2009).

Finally, we anticipate that the MWA will be upgraded to add a further 128 tiles, roughly doubling the current array resolution. As a result, the classical confusion noise at 154 MHz will decrease by a factor of $\approx 5-10$ depending on the slope of the source counts below 6 mJy. The sidelobe levels are also expected to decrease, which will further reduce sidelobe confusion. This raises the possibility of conducting large-area, sub-mJy continuum surveys, particularly at the higher MWA observational frequency range ($\approx$ 200 MHz).

ACKNOWLEDGMENTS

This work makes use of the Murchison Radioastronomy Observatory, operated by CSIRO. We acknowledge the Wajarri Yamatji people as the traditional owners of the Observatory site. We thank the anonymous referee for their suggestions, which have improved this paper. CAJ thanks the Department of Science, Office of Premier & Cabinet, WA for their support through the Western Australian Fellowship Program. Support for the MWA comes from the U.S. National Science Foundation (grants AST-0457585, PHY-0835713, CAREER-0847753, and AST-0908884), the Australian Research Council (LIEF grants LE0775621 and LE0882938), the U.S. Air Force Office of Scientific Research (grant FA9550-0510247), and the Centre for All-sky Astrophysics (an Australian Research Council Centre of Excellence funded by grant CE110001020). Support is also provided by the Smithsonian Astrophysical Observatory, the MIT School of Science, the

Table 2. Parameter values adopted to model the 154 MHz counts with the resultant predicted classical and sidelobe confusion noise assuming a beam size of 2.31 arcmin.

Model	k_1	γ_1	k_2	γ_2	$S_{\rm low}$ (mJy)	$S_{\rm mid}$ (mJy)	$S_{\rm high}$ (mJy)	$\sigma_{\rm c}$ (mJy/beam)	$\sigma_{\rm s}$ (mJy/beam)
A	6998	1.54	6998	1.54	0.1	6.0	400	1.7	3.5
B	1841	1.800	6998	1.54	0.1	6.0	400	1.7	3.5
C	661.8	2.000	6998	1.54	0.1	6.0	400	1.8	3.4
D	237.9	2.200	6998	1.54	0.1	6.0	400	2.0	3.4

Table 3. Predicted source densities at 154 MHz for various detection limits for each source count model explored in Section 6.

$S_{\rm lim}$ / mJy/beam	N / deg^2 for model A	N / deg^2 for model B	N / deg^2 for model C	N / deg^2 for model D
5.00	62	62	63	63
1.00	157	190	224	268
0.50	231	320	425	580
0.10	560	1125	2038	3838
0.03	1077	2925	6742	16187

Raman Research Institute, the Australian National University, and the Victoria University of Wellington (via grant MED-E1799 from the New Zealand Ministry of Economic Development and an IBM Shared University Research Grant). The Australian Federal government provides additional support via the Commonwealth Scientific and Industrial Research Organisation (CSIRO), National Collaborative Research Infrastructure Strategy, Education Investment Fund, and the Australia India Strategic Research Fund, and Astronomy Australia Limited, under contract to Curtin University. We acknowledge the iVEC Petabyte Data Store, the Initiative in Innovative Computing and the CUDA Center for Excellence sponsored by NVIDIA at Harvard University, and the International Centre for Radio Astronomy Research (ICRAR), a Joint Venture of Curtin University and The University of Western Australia, funded by the Western Australian State government.

REFERENCES

Beardsley A. P. et al., 2013, MNRAS, 429, L5
Bernardi G. et al., 2009, A&A, 500, 965
Bowman J. D. et al., 2013, PASA, 30, e031
Bridle A. H. & Schwab F. R., 1999, Synthesis Imaging in Radio Astronomy II, 180, 371
Calabretta M. R., Staveley-Smith L., Barnes D. G., 2014, PASA, 31, e007
Condon J., 1974, ApJ, 188, 279
Condon J. J., Cotton W. D., Greisen E. W., Yin Q. F., Perley R. A., Taylor G. B., Broderick J. J., 1998, AJ, 115, 1693
Chapman E. et al., 2012, MNRAS, 423, 2518
Condon J. J. et al., 2012, ApJ, 758, 23
Dewdney P. et al., 2010, SKAMemo #130, SKA Phase 1: Preliminary System Description, www.skatelescope.org/publications/
Edge D. O., Shakeshaft J. R., McAdam W. B., Baldwin J. E., Archer S., 1959, MNRAS, 68, 37
Fomalont E. B., Bridle A. H., Davis M. M., 1974, A&A, 36, 273
Gehrels N., 1986, ApJ, 303, 336
Ghosh A., Prasad J., Bharadwaj S., Ali S. S., Chengalur J. N., 2012, MNRAS, 426, 3295
Gower J. F. R., 1966, MNRAS, 133, 151
Hales S. et al., 2007, MNRAS, 382, 1639
Hales C. A. et al., 2014, MNRAS, 441, 2555
Hancock P. et al., 2012, MNRAS, 422, 1812
Harker G. et al., 2010, MNRAS, 405, 2492
Hopkins A. M., Afonso J., Chan B., Cram L. E., Georgakakis A., Mobasher B., 2003, AJ, 125, 465
Hurley-Walker N. et al., 2014, PASA, 31, e045
Huynh M. T., Jackson C. A., Norris R. P., Prandoni I., 2005, AJ, 130, 1373
Intema H. T., van Weeren R. J., Röttgering H. J. A., Lal D. V., 2011, A&A, 535, A38
Jackson C. A., Wall J. V., 1999, MNRAS, 304, 160
Jackson C., 2005, PASA, 22, 36
Kellermann K. I., 1964, ApJ, 140, 969
Loi S. T. et al., 2015, Radio Science, 50, 574
Longair M. S., 1966, MNRAS, 133, 421
Lonsdale C. J. et al., 2009, Proc. IEEE, 97, 1497
Mauch T., Murphy T., Buttery H. J., Curran J., Hunstead R. W., Piestrzynski B., Robertson J. G., Sadler E. M., 2003, MNRAS, 342, 1117
Mitchell K. J., Condon J. J., 1985, AJ, 90, 1957
Mitchell D. A., Greenhill L. J., Wayth R. B., Sault R. J., Lonsdale C. J., Cappallo R. J., Morales M. F., Ord S. M., 2008, IEEE Journal of Selected Topics in Signal Processing, 2, 707
Morales M. F., Hewitt J., 2004, ApJ, 615, 7
Offringa A. R. et al., 2014, MNRAS, 444, 606
Offringa A. R. et al., 2015, PASA, 32, 8
Offringa A. R. et al., 2016, MNRAS, submitted
Ord S., Greenhill L., Wayth R., Mitchell D., Dale K., Pfister H., Edgar R., 2009, ASPC, 411, 127
Parsons A. R. et al., 2014, ApJ, 788, 106
Scheuer P. A. G., 1957, Proceedings of the Cambridge Philosophical Society, 53, 764
Sullivan I. S. et al., 2012, ApJ, 759, 17
Thyagarajan N. et al., 2013a, ApJ, 776, 6
Thyagarajan N., 2013b, Notes on MWA 128T confusion limits, MWA Technical Memo. Available at: http://mwa-lfd.haystack.mit.edu/knowledgetree/view.php?fDocumentId=826
Tingay S. J. et al., 2013, PASA, 30, e007

Toffolatti L., Argueso Gomez F., de Zotti G., Mazzei P., Franceschini A., Danese L., Burigana C., 1998, MNRAS, 297, 117
Trott C. M., Wayth R. B., Tingay S. J., 2012, ApJ, 757, 101
van Haarlem M. P. et al., 2013, A&A, 556, A2
Wall J. V., 1994, AuJPh, 47, 625
Wayth R. B. et al., 2015, PASA, 32, e025
White R. L., Becker R. H., Helfand D. J., Gregg M. D., 1997, ApJ, 475, 479
Wieringa M., 1991, PhD thesis, Leiden University
Williams W. L., Intema H. T., Röttgering H. J. A., 2013, A&A, 549, A55
Zwart J. et al., 2015, in Bourke T. L. et al., eds, Proc. Advancing Astrophysics with the Square Kilometre Array, Astronomy below the Survey Threshold, id. 172. Available at: http://pos.sissa.it/cgi-bin/reader/conf.cgi?confid=215#session-2110

APPENDIX A: EXTRAPOLATING THE 1400 MHz COUNTS TO PREDICT THE 154 MHz SKY

Fig. A1 shows counts in the frequency range 154–178 MHz extrapolated to 154 MHz compared with 1400 MHz counts extrapolated to 154 MHz, in all cases assuming a spectral index of –0.75. It can be seen that extrapolation of the 1400 MHz counts to 154 MHz significantly overpredicts the 154 MHz counts below about 500 mJy. The density of sources at S_{154} = 6 mJy is overpredicted by about a factor of two.

Moreover, Fig. A2 shows that the 154 MHz counts above 6 mJy cannot be accurately reproduced from extrapolation of the 1.4 GHz counts using *any* spectral index; the best fit is obtained for a spectral index of –0.75. A polynomial fit to the 154 MHz counts is compared with a polynomial fit to the 1400 MHz counts extrapolated to 154 MHz assuming a spectral index of –0.90, –0.80, –0.75, –0.70 and –0.60. The integral of the squared difference between the two curves from S_{154} = 6 mJy to S_{154} = 100 Jy is minimised for $\alpha = -0.75$.

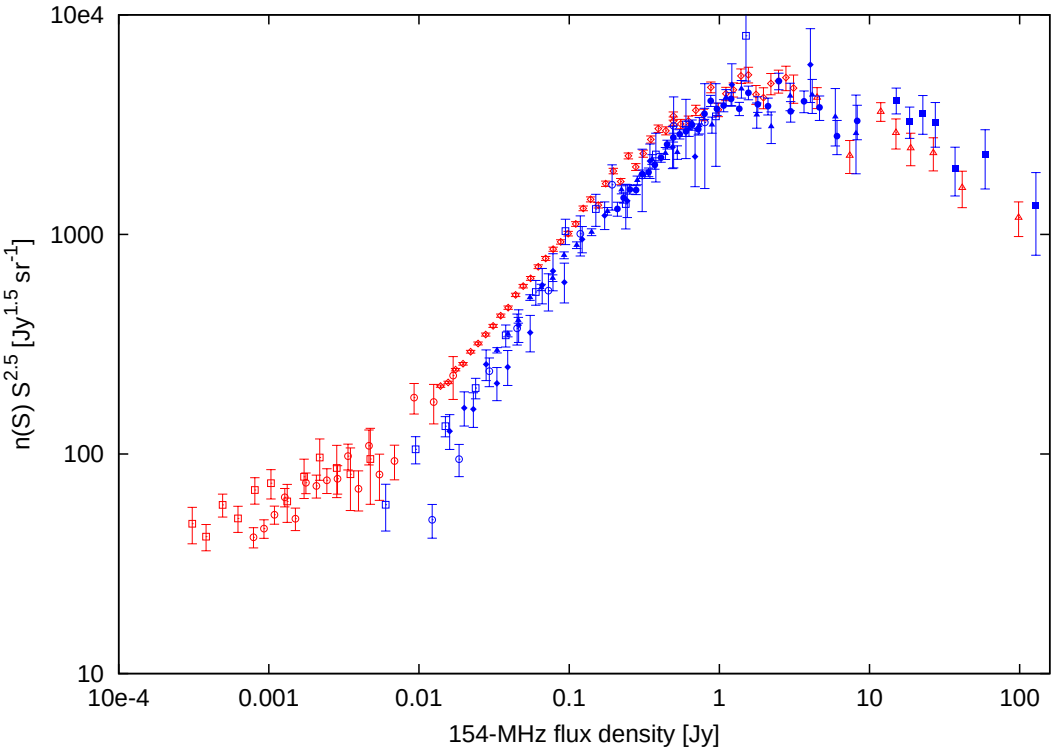

Figure A1. Comparison of counts in the frequency range 154–178 MHz extrapolated to 154 MHz (blue) with 1400 MHz counts extrapolated to 154 MHz (red), in all cases assuming $\alpha = -0.75$. The data sources are as follows. 154 MHz: filled circles, Hales et al. (2007); filled triangles, this paper; filled lozenges, Williams, Intema & Röttgering (2013); open squares, Intema et al. (2011); open circles, Ghosh et al. (2012); 178 MHz extrapolated to 154 MHz: filled squares, Edge et al. (1959); 1400 MHz extrapolated to 154 MHz: open circles, Hales et al. (2014); open squares, Huynh et al. (2005); open triangles, Fomalont, Bridle & Davis (1974); open lozenges, White et al. (1997).

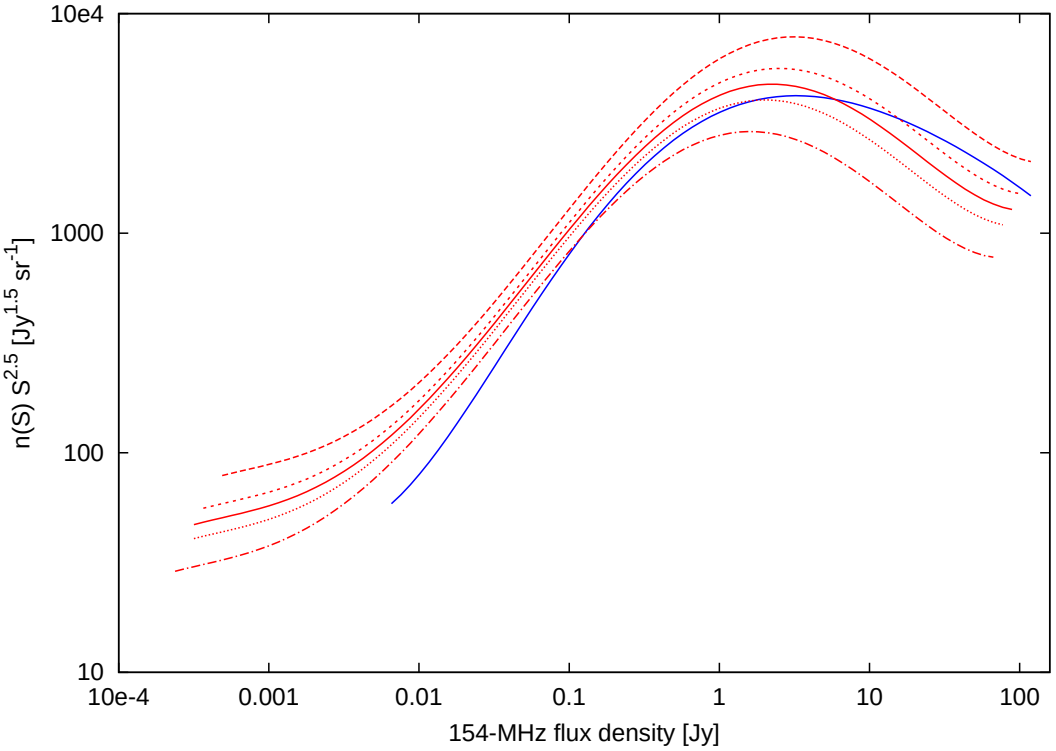

Figure A2. Polynomial fit to the 154 MHz counts (blue). Polynomial fit to the 1.4 GHz counts extrapolated to 154 MHz assuming $\alpha = -0.90$ (red dashed line), $\alpha = -0.80$ (red hashed line), $\alpha = -0.75$ (red solid line), $\alpha = -0.70$ (red dotted line) and $\alpha = -0.60$ (red dot-dashed line).